High-Fidelity Numerical Analysis of Per-Rev-Type Inlet Distortion Transfer in Multistage Fans—Part I: Simulations With Selected Blade Rows

Jixian Yao
GE Global Research,
One Research Circle,
Niskayuna, NY 12309

Steven E. Gorrell
Department of Mechanical Engineering,
Brigham Young University,
435 CTB, Provo, UT 84602

Aspi R. Wadia
GE Aviation,
30 Merchant Street, P20,
Cincinnati, OH 45215

Demands for improved performance and operability of advanced propulsion systems require an understanding of the physics of inlet flow distortion transfer and generation and the subsequent engine response. This also includes developing a high-fidelity characterization capability and suitable tools/rules for the design of distortion tolerant engines. This paper describes efforts to establish a high-fidelity prediction capability of distortion transfer and fan response via high-performance computing. The current CFD capability was evaluated with a focus of predicting the transfer of prescribed inlet flow distortions. Numerical simulations, comparison to experimental data, and analysis of two selected three-stage fans are presented. The unsteady Reynolds-Averaged Navier-Stokes (RANS) code PTURBO demonstrated remarkable agreement with data, accurately capturing both the magnitude and profile of total pressure and total temperature measurements. Part I of this paper describes the establishment of the required numerical simulation procedures. The computational domains are limited to the first three blade rows for the first multistage fan and the last three blade rows for the second fan. This paper presents initial validation and analysis of the total pressure distortion transfer and the total temperature distortion generation. Based on the established ground work of Part I, the entire two multistage fans were simulated with inlet distortion at normal operating condition and near stall condition, which is Part II of this paper. Part II presents the full range validation against engine test data and in-depth analysis of distortion transfer and generation mechanisms throughout the two fans. [DOI: 10.1115/1.3148478]

1 Introduction

The fan and compressor of a modern aircraft engine are seldom run in a uniform inlet flow field after entering service. Ever since the early days of aircraft engine installations, the effects of distorted inflow and incoming turbulence to gas turbine engines have been a concern. This concern is more pronounced as increasingly advanced aircraft are designed for a wide range of operations and high fuel efficiency. Inlet distortion influences engine stability, performance, and structural integrity, manifested by an inability to accelerate, engine overheating, compressor stall and surge, or combustion flame out. The engine must work with and tolerate the inlet distortion since it cannot be completely eliminated due to aircraft installation effects. A common design strategy is to match a compressor stage well below its peak pressure ratio, in order to gain higher stability margin during distorted operation.

Current design methodology and modeling techniques for distortion in the aviation and engine industry was developed during the 1960s to 1970s based on empirical correlations [1–4]. These include the parallel compressor model and its extensions and modifications, especially for the discovery of critical angle of spoiled sectors for steady-state circumferential distortions. The modeling of distortion transfer and evaluation of inlet distortion effects continued to flourish throughout the late 20th century to this day. The most commonly known contribution was the

Greitzer–Hynes model [5,6] in the late 1980s. This model and its later extensions [7–9] for compressibility are still the guide in today's fan/compressor design process. The challenges today, however, are increasingly advanced three-dimensional design of low-aspect ratio fans and compressors. The distortion patterns include not only total pressure distortions but also total temperature distortions and swirl distortions. These distortions, in real operating conditions, are often time variant as well. The distortions in pressure, temperature, and swirl interact with each other in a highly nonlinear fashion. A higher fidelity understanding of distortion transfer and fan response is the driving force for development of appropriate analytical tools that model stage-by-stage distortion transfer behavior, as well as fan blade loading variations in the circumferential direction.

Over the past decade, a great wealth of insights of unsteady flow physics in gas turbine engines was gained through experiments and computational fluid dynamics (CFD). As the capability of parallel computing and processor speed have steadily increased, numerical simulations play an increasingly important role in discovering the physics of unsteady flows in turbomachinery, such as blade row interactions, tip and hub clearance flows, hot streak migration in turbines, and endwall contouring. CFD, often regarded as the "third way" aside from physical experiments and traditional theoretical analysis, is suitable to meet the challenges described above. CFD simulations for inlet distortion transfer and fan response have started to emerge in the late 1990s. Hirai et al. [10] calculated a single turbine stage for inlet temperature distortion and an isolated fan rotor for inlet pressure distortion. Gong [11] developed a simplified CFD model for rotating stall inception and inlet distortion in multistage compressor. Hale et al. [12] coupled the inlet component and a three-stage fan using CFD,

---

with the fan being modeled with source terms (blade forces and shaft work) from streamline curvature solutions. Chima [13] performed CFD simulations of the NASA stage 35 for compressor stability. Meanwhile, reduced-order modeling for inlet distortion continues to develop. Ryman et al. [14] studied the Volterra model for pressure distortion on high-cycle fatigue. Cousins [15] described the improved modeling for a high-bypass ratio fan. These models are of great value for operability studies, and they are bridges between high-fidelity CFD and the design process, through which the gains in flow physics can then be realized and applied to design better engines.

This paper presents the initial step toward a high-fidelity CFD capability. Previous modeling efforts [5,11–13,15] have largely focused on understanding the impact of inlet distortion on stall margin. This high-fidelity CFD effort is unique in its attempt to evaluate the ability to model inlet distortion and determine if it is a tool capable of predicting distortion transfer and generation in multistage turbomachinery. Two high-performance multistage fans were modeled for this research. Each of these fans consists of an IGV and three stages, with engine test data to validate the CFD procedure. Instrumentation was placed at stator vane leading edges as well as at the fan inlet and exit. Total pressure and total temperature were measured at five immersions. Some casing static pressure measurements were available as well. The motivation for this work is a desire to design distortion tolerant fans and accurately predict the inlet conditions to the core compressor. The front block (first three blade rows) of the first fan and the rear block of the second fan (last three blade rows), full annulus for each blade row, were simulated. The reason for this selection is to gain higher confidence in numerical predictions. The two fans were designed quite differently. The numerical simulation is subjected to total pressure distortion only for the front block of the first fan, and to both total pressure and total temperature distortions for the rear block of the second fan. Besides the validation of the CFD prediction, the simulations are analyzed to understand the physics of temperature distortion generation and transfer. Accurate prediction of total temperature distortion is important as it affects the corrected speed for downstream rotors and flow capacity of stators. The level of temperature distortion to the core compressor is also an important factor since the temperature distortion is usually amplified as the fan attenuates the pressure distortion. The temperature distortion is generated as the first fan rotor that responds to the incoming total pressure distortion and is found to have significant spatial phase difference (in the circumference) relative to the total pressure distortion. This paper explains how the total temperature distortion phasing is generated in the first fan model and how that phase changes as the distortion transfers in the second fan model.

This paper is divided into sections discussing the boundary conditions, the computational challenges, the analysis of the CFD results, and the comparison of numerical results against test data.

2 Computational Approach

This section describes the CFD flow solver, the computational domains, and the boundary conditions at inlet and exit.

2.1 Flow Solver. The flow solver chosen was the unsteady Reynolds-Averaged Navier-Stokes (RANS) code, PTURBO [16,17], developed by Dr. Jenping Chen with support from NASA, Industry, and the DoD. Its solution algorithm is an implicit finite volume solver that incorporates Newton subiterations and a block-Jacobi Gauss–Seidel relaxation scheme at each physical time step. It has a third-order accurate monotonic upstream-centered schemes for conservation laws (MUSCL)-type of spatial discretization scheme coupled with a second-order accurate temporal discretization, which helps to improve flow resolution and minimize dispersion error. Turbulence modeling is accomplished via the NASA/CMOTT k-epsilon model specifically developed for turbomachinery flows. This code was modified by GE to accept distor-
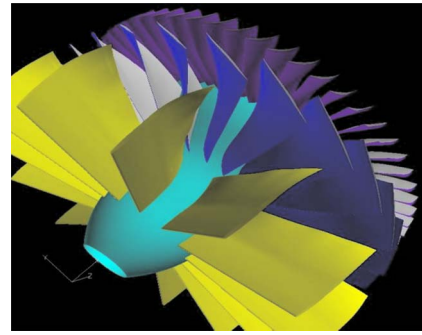

Fig. 1   Computational domain of Fan Model 1

tion boundary conditions at inlet and exit boundaries. With predetermined load balancing, this flow solver has demonstrated high scalability and parallel efficiency.

2.2 Fan Model 1. The first fan consists of three stages with an IGV. For evaluation of the computational approach, the front block of the fan, shown in Fig. 1, was modeled. The domain includes the IGV and the first stage. This was deemed sufficient for the purpose of assessing the CFD prediction capability with a moderate requirement of computing resources. It also helped to identify and work out challenges with the CFD procedure.

The computational domain consists of the IGV, Rotor-1 and Stator-1, and full annulus for each blade row. Blade counts are 13 IGVs, 24 Rotor-1 blades, and 62 Stator-1 vanes. Grid size for one IGV passage is $221 \times 231 \times 65$ in the axial, tangential, and radial directions. For the Rotor-1, the grid per passage is $227 \times 125 \times 65$, and for the Stator-1, the grid is $171 \times 49 \times 65$ per passage. The IGV and the Stator-1 were properly clocked to engine test position. The inlet total pressure was a 1/rev sinusoidal distribution measured from the engine test. Also adopted from the engine test were total temperature and flow angles. The total temperature and flow angles were uniformly distributed in the circumference but with radial profiles. Figure 2(a) shows the absolute total pressure distribution at inlet. The peak-to-peak total pressure distortion at inlet is about 20% of the circumferential mean. The exit boundary condition downstream of Stator-1 was more difficult to specify. The pressure distortion was not expected to attenuate at this location, and the engine test only had readings at hub and casing, with none in-between. The static pressure radial profile at this location was taken from the data-matched through-flow solution and was scaled to measurements from the hub and casing. The resulting exit boundary condition distribution is shown in Fig. 2(b). It is necessary to point out that the hub pressure probes were located within the hub cavity instead of being on the hub surface. This may drive the CFD prediction near the hub to a different flow pattern than expected.

2.3 Fan Model 2. The second fan also consists of three stages with an IGV. This fan has higher wheel speed and higher overall pressure ratio than the first one. Work split among the three stages was also different than the first one. For this simulation, the computational domain consisted of the rear three blade rows (Stator-2, Rotor-3, and Stator-3) and a section of flowpath downstream of Stator-3. Blade counts were 108, 50, and 118, respectively. The inlet boundary conditions were developed from experimental data obtained with a 180/rev inlet total pressure distortion at +10% operating line. The Stator-2 inlet inflow had both total pressure and total temperature distortions. This is in contrast to the first fan model, which had only total pressure distortion at inlet. A sinusoidal function was fitted through the Stator-2 leading edge data using

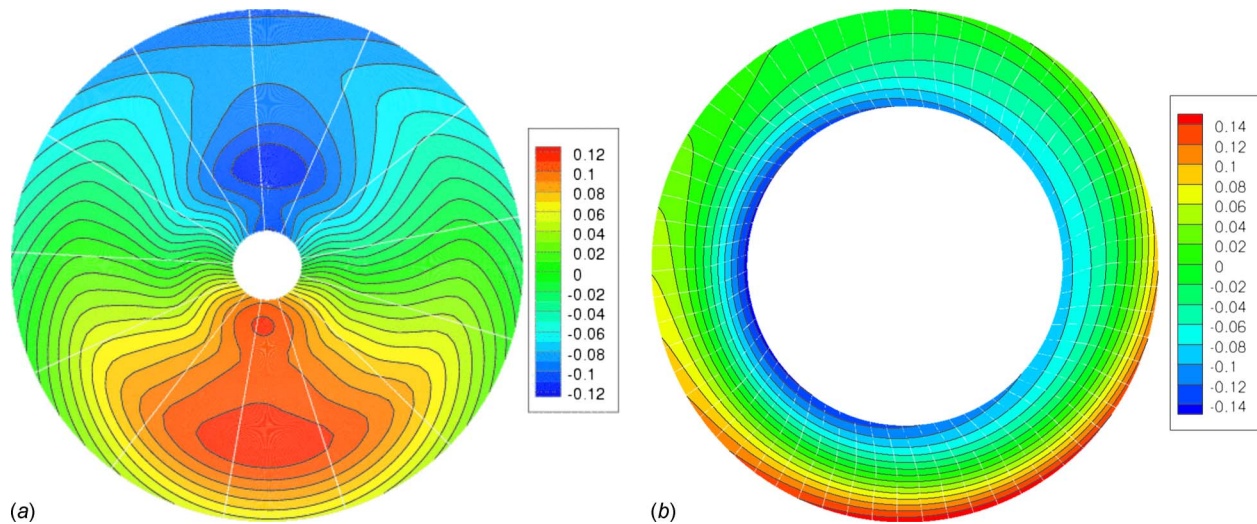$$Pt = Pt_{\text{ave}} \cdot (1 + \text{amp}\_{Pt} \cos(\text{phase}\_{Pt} + \theta)) \qquad (1)$$

Fig. 2 Boundary conditions for Fan Model 1. 1/rev total pressure distortion at inlet (*a*), and the static pressure distribution at Stator-1 exit (*b*). $[(Pt - \bar{P}t)/\bar{P}t]\%$ is plotted in (*a*), and $[(Ps - \bar{P}s)/\bar{P}s]\%$ is plotted in (*b*).

$$Tt = Tt_{\text{ave}} \cdot (1 + \text{amp}\_Tt \cos(\text{phase}\_Tt + \theta)) \qquad (2)$$

The boundary condition was specified at six immersions (8.9%, 27.3%, 46.6%, 67%, 88.6%, and 94.3%). The amplitudes and phase are functions of span. Contour plots of the inlet boundary condition for the second fan are shown in Figs. 3(*a*) and 3(*b*).

The domain for each Stator-2 passage was $153 \times 73 \times 57$ in the axial, tangential, and radial directions. For Rotor-3, $149 \times 73 \times 81$ nodes were used and the Stator-3 domain was $215 \times 73 \times 57$ nodes. The total nodes were therefore 218,372,784, which were split into 444 blocks to run the simulation.

These two carefully selected computational domains are complementary to each other to cover a broader range in the effort of assessing the CFD capabilities.

3 Computational Challenges

The first challenge was to determine the appropriate level of details to resolve. The 1/rev distortions have a much longer wavelength than that of blade row interactions, and are inviscid in nature. This can be resolved using a fairly coarse grid. However,

this is not the factor for determining the CFD fidelity level. Blade row interactions, wake migration, and viscous boundary layers must also be resolved properly because the imposed distortion interacts with all these high frequency perturbations in a highly nonlinear fashion. On the other hand, the fidelity level is also limited by the computing resources and the required turn-around time. The stator row, which has most of the vanes, was used as a benchmark for grid resolution. A grid of 700,000 cells was determined to be appropriate to satisfy the above-mentioned criteria based on time-accurate CFD experience and trial calculations. This assessment was based on the third-order spatial accuracy that PTURBO has. Grid density was then maintained for all other rows. Besides the regular clustering of cells in the viscous layers and in hub/tip clearance regions, special attention was taken to ensure proper grid resolution in the regions outside viscous layers to resolve pressure and shock wave propagation. Smooth grid resolution was necessary in the circumferential direction near the vicinity of the sliding mesh interface to avoid interpolation errors. Furthermore, smooth grid resolution was also needed in the axial
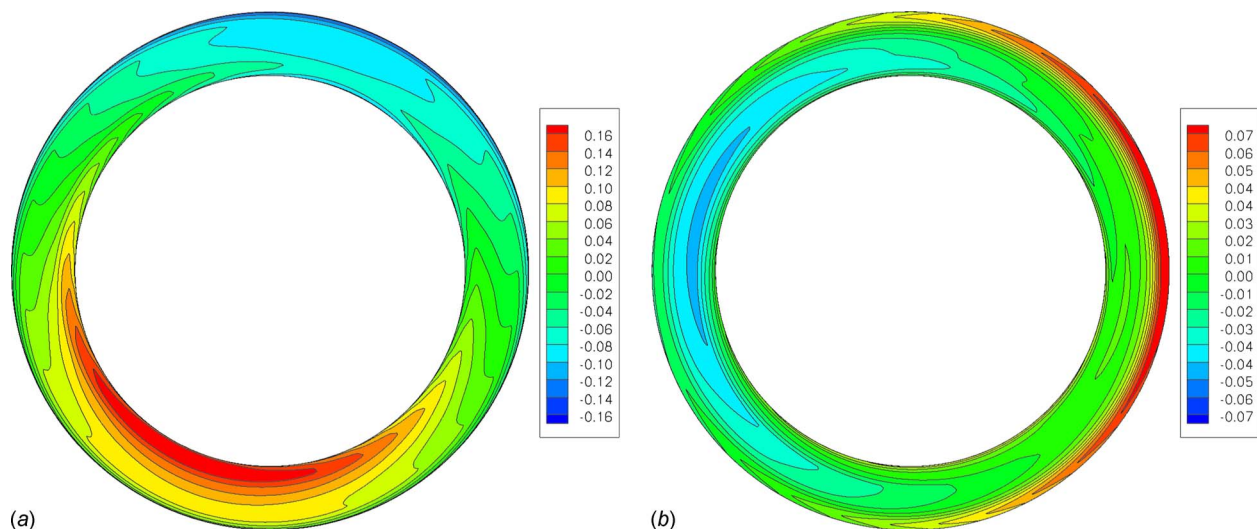

Fig. 3 Inlet boundary conditions for Fan Model 2. 1/rev total pressure distortion at inlet to Stator-2 (*a*), and the total temperature distortion at inlet to Stator-2 (*b*). $[(Pt - \bar{P}t)/\bar{P}t]\%$ is plotted in (*a*), and $[(Tt - \bar{T}t)/\bar{T}t]\%$ is plotted in (*b*).

direction across the sliding mesh interface to minimize loss of flow features, such as shock waves and wakes.

Several challenges were also addressed related to the CFD flow solver. The first was that the overall initial solution had to be a fairly good one, at least for the pressure distribution throughout the domain. This was achieved using the solution from GE's through-flow code, which provided an axisymmetric solution. The other aspect was the robustness of the time marching scheme. The Newton iteration employed in the flow solver required a close initial guess while providing rapid convergence. However, there was no way to guarantee this everywhere in the flow field, especially in regions where flow properties had a large rate of change such as hub and tip clearances. This often led to an unexpected crash of the flow solver. A slight change of grid in those regions could help but it was a trial-and-error approach. Intuitively, increase in grid density in those regions may help, but in reality it often made it worse. To alleviate this challenge, increasing the number of steps per period proved helpful as the factorization error and linearization error in the LU-SGS procedure are directly linked to the size of the physical time step. In comparison to the alternative algorithm, dual-time stepping, in solving the unsteady RANS, the implicit LU-SGS procedure provides a nominal second-order accuracy in time derivatives, but often requires smaller time step than that can be tolerated by the dual-time stepping. Large time steps in the direct implicit algorithm would result in accumulation of those factorization and linearization errors associated only with the direct implicit algorithm.

Yet another challenge was found when establishing boundary conditions. The inlet and exit boundary condition treatment in today's CFD solvers still uses one-dimensional Riemann invariants based on characteristics of the flow equations, or the traveling direction of information from a physics perspective, determined by the eigenvalues of the inviscid Jacobian matrices of the flow equations. Flow reversal at the inlet and exit boundary would sooner or later cause a stability issue, simply because the reversed flow is not consistent with the characteristic based boundary condition treatment. On the other hand, nonreflecting boundary conditions for both inlet and exit are desired for this kind of calculations due to the lack of freedom to choose the location of the inlet and exit boundaries. It's either dictated by the underlying configuration or limited by the capability of the flow solver.

All the numerical simulations were carried out at the Aeronautical Systems Center, Major Shared Resource Center (ASC MSRC) running on an SGI Origin 3900 and SGI Altix B×2.

4 CFD Results for Fan Model 1

This section presents the CFD results of the front block (first three blade rows) of the first fan model. Comparisons with available engine test data are discussed. The flow properties are non-dimensionalized using $\hat{f} = (f - f_{ref,min})/(f_{ref,max} - f_{ref,min})$. The location of reference values in this section are taken from the Stator-1 leading edge on the hub surface. Exceptions are stated with each plot in this section.

4.1 Generation of Total Temperature Distortion. The temperature distortion generation was expected as a result of fan response to the pressure distortion. The interesting aspect is not the generation itself; rather, it is the relative phasing difference between the generated temperature distortion and the incoming pressure distortion. Figure 4 shows a snapshot at one instant in time of the absolute total pressure and total temperature at midspan of the flow field. The domain is unwrapped to show the whole circumferential view of the flow. The flow comes in from bottom, and goes up through the IGV and the first fan stage. The rotor rotates from right to left. The positive theta direction is the same as the rotation, and is clockwise aft looking forward. The total pressure distortion went through the first fan stage, staying in phase (relative to the phase at inlet of IGV). The total temperature distortion was generated within the rotor passages, and had about a 90 deg
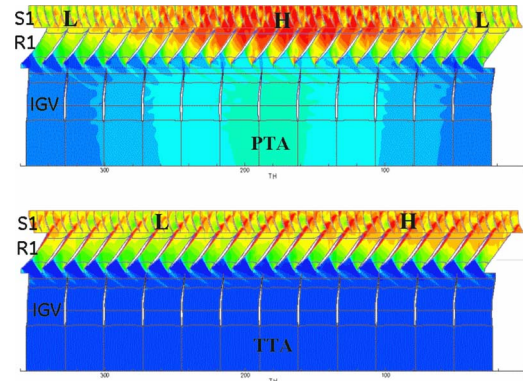

Fig. 4 Time-accurate solution of absolute total pressure and total temperature distribution at midspan on unwrapped surface

phase difference to the total pressure distortion, lagging in the direction of rotation. This temperature distortion propagated through the stator passages without additional phase change. Figure 5 shows the comparison at this span between the predicted total pressure and total temperature and the measured values. The CFD simulation predicted the generation of the temperature distortion, and more importantly the phase difference. Validating PTURBO's ability to model the phasing difference is important because it amounts to the prediction of the Rotor-1 response to the incoming pressure distortion. This is significant since due to the temperature variation, the downstream rotors operate at different corrected speed at different circumferential locations. Flow into the downstream stators are affected as well.

4.2 Comparison to Test Data. The CFD results presented in this section underline the fact that inlet total pressure distortion alone can generate total temperature distortion as a fan rotor response and swirl distortion driven by static pressure variation in the circumference.

4.2.1 Profiles of Total Pressure and Total Temperature. Besides the above-mentioned comparison at midspan (Fig. 5), there are other immersions where PT and TT data were available. The PT and TT probes were mounted on the leading edge of the stator. Two stator vanes were instrumented, which were located at 128 deg and 331 deg, respectively. There were 13 readings available, corresponding to 13 distortion screen locations. Figures 6–9 present comparisons of all the available PT and TT data against
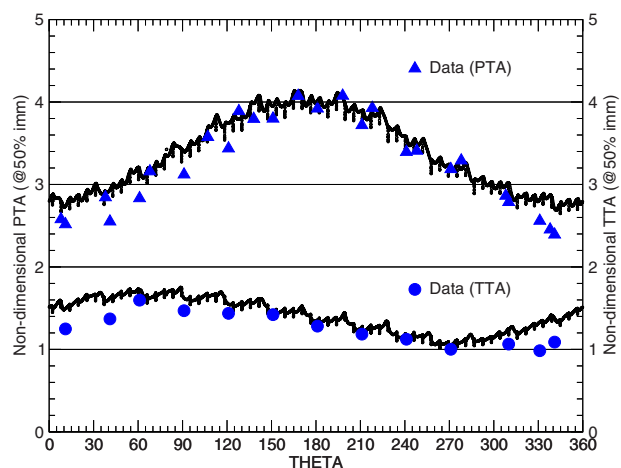

Fig. 5 Comparison of absolute total pressure (PTA) and total temperature (TTA) at midspan, Stator-1 inlet
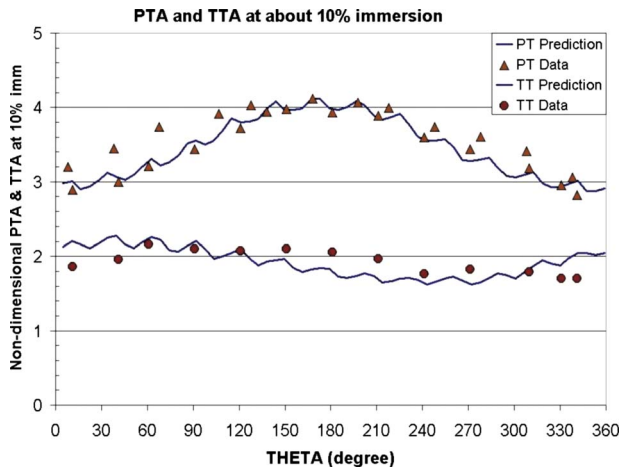
Fig. 6 Comparison of absolute total pressure and total temperature at Stator-1 inlet, about 10% immersion

Fig. 8 Comparison of absolute total pressure and total temperature at Stator-1 inlet, about 70% immersion

the CFD results. The sampling locations of the CFD results did not exactly match the probe locations, which were not available. The CFD samples were energy averaged for PT and mass averaged for TT. The circumferential profiles in these plots were "passage averaged" and are plotted in nondimensional values.

At about 10% immersion (Fig. 6), the predicted total pressure profile matches data well. For the total temperature, the predicted profile represents a sinusoidal-like form that shifts away from the measured profile. It was noted that at this location, only one of the two TT probe readings was meaningful. Increased resolution of the tip gap flow might be necessary to improve the total temperature prediction. At about 30% immersion (Fig. 7), the PT profiles match the data as well. The total temperature data show a better sinusoidal form than at 10% immersion, and the CFD prediction matches the data well, though the overall magnitude of CFD is slightly lower (about 1%). At about 70% immersion (Fig. 8), only one probe had meaningful readings for total pressure (PT), and the prediction still matched the data. The total temperature again has a sinusoidal form, and the prediction matched the data. The overall level of prediction however was higher (about 1.5%), contrary to that at 30% immersion. Recall from Sec. 3, that at midspan, both the level and the shape of the profile compared very well with data. At 90% immersion near the hub (Fig. 9), the predicted total pressure level was higher (about 8%) than data, but the prediction
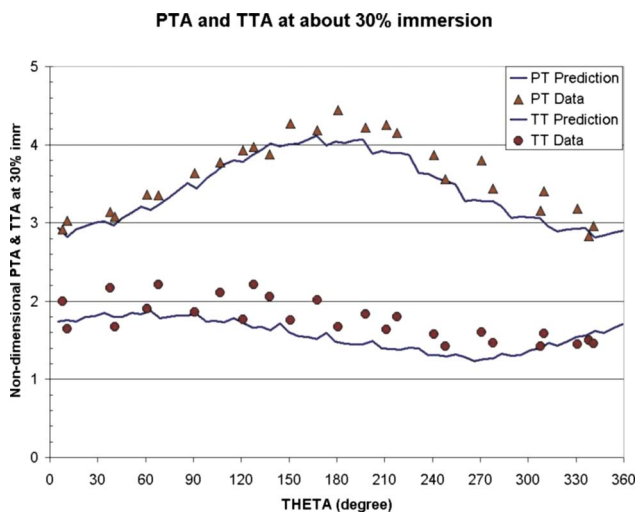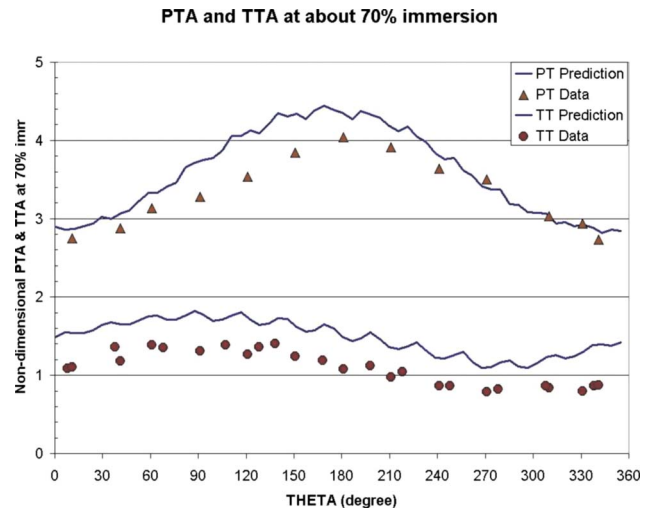
still held the profile shape very well. The predicted total temperature also matched the profile well, but the overall level was higher (about 1.5%), similar to that at 70% immersion. The overall PT and TT level translates to the spanwise profiles that are commonly used for comparison in steady-state and time-averaged calculations. This generally reflects the spanwise profile prediction accuracy of the current RANS (or URANS) CFD capability.

4.2.2 Casing Statics. The casing statics upstream and downstream of Rotor-1 were also compared in Fig. 10. The good agreement between the CFD and the data in both the overall level and the profile shape indicates that the pressure rise across the rotor is accurately captured near the casing by the simulation.

5 CFD Results for Fan Model 2

A snapshot in time of the 3D simulation near 50% immersion is shown in Fig. 11 for total pressure and Fig. 12 for total temperature. As seen in these figures as well as Figs. 3(a) and 3(b), an approximately 90 deg phase shift already exists between the total pressure and total temperature at the inlet to Stator-2. These were imposed as inlet boundary conditions. Figures 11 and 12 show that no additional phase shift occurs for total pressure distortion
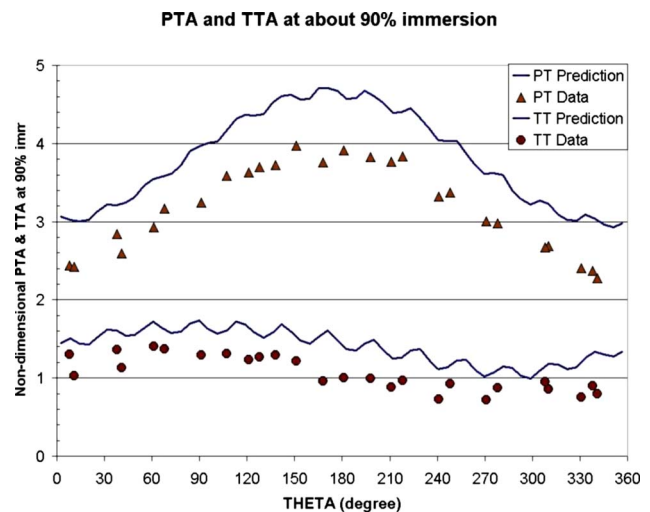

Fig. 7 Comparison of absolute total pressure and total temperature at Stator-1 inlet, about 30% immersion

Fig. 9 Comparison of absolute total pressure and total temperature at Stator-1 inlet, about 90% immersion

Journal of Turbomachinery

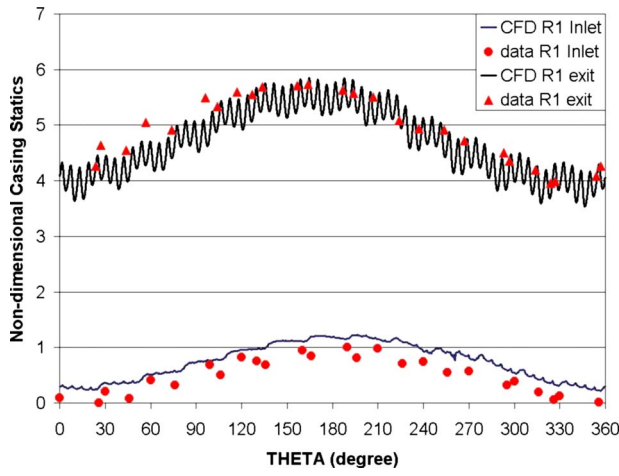OCTOBER 2010, Vol. 132 / **041014-5**

Fig. 10 Comparison of casing static pressure at upstream and downstream of the Rotor-1. Reference pressure (used for non-dimensionalization) location is Rotor-1 inlet on casing.

Fig. 13 Comparison of calculated *Pt* and *Tt* profiles with data at 91% immersion

through Stator-2, Rotor-2, and Stator-3. However, there is a slight phase shift (about 25 deg) for total temperature, which occurs within Rotor-3 passage. No additional phase shift occurs across Stator-3 for total temperature at this immersion.

Validation of the CFD simulation of the second fan model was accomplished by comparing the simulation with experimental data acquired at exit rakes downstream of Stator-3. Figures 13–15 compare the total pressure and total temperature numerical predictions with experimental data at 91%, 55%, and 7.3% immersions.
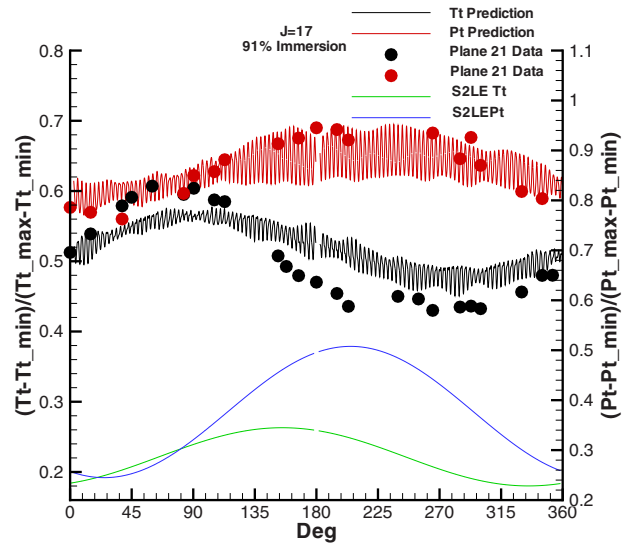
The data have been nondimensionalized. The data match is considered excellent. Generally the simulation predicted total pressure values very near the measured data. Where differences do exist they are small (between 2.5% and 3.5%). The simulation captured the total pressure profile accurately also. The total temperature profile and magnitude was captured accurately as well. Any differences in magnitude were only between 1.2% and 3.3%.
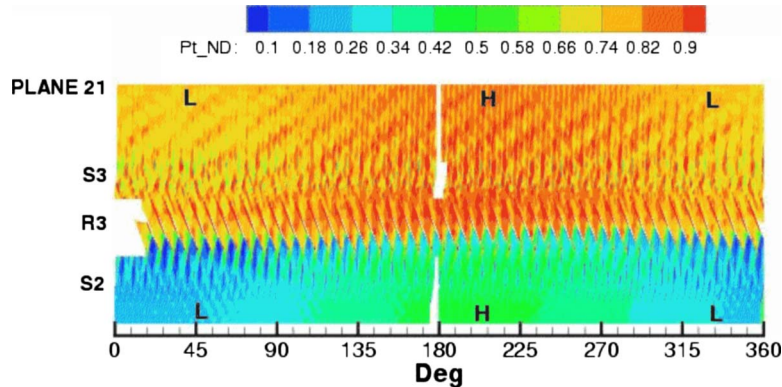

Fig. 11 Absolute total pressure distribution, snapshot of time-accurate solution at about 50% immersion
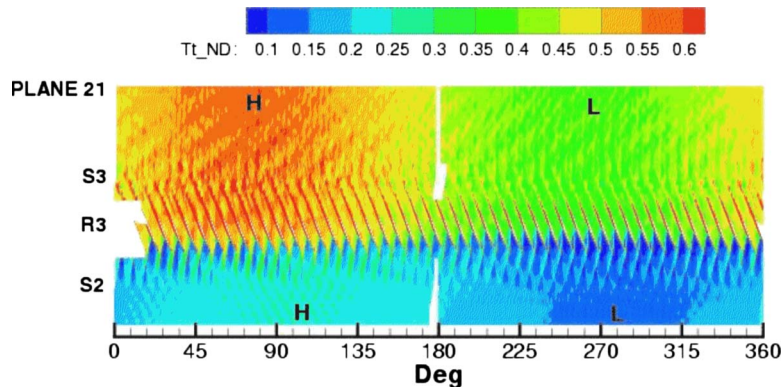

Fig. 12 Absolute total temperature distribution, snapshot of time-accurate solution at about 50% immersion
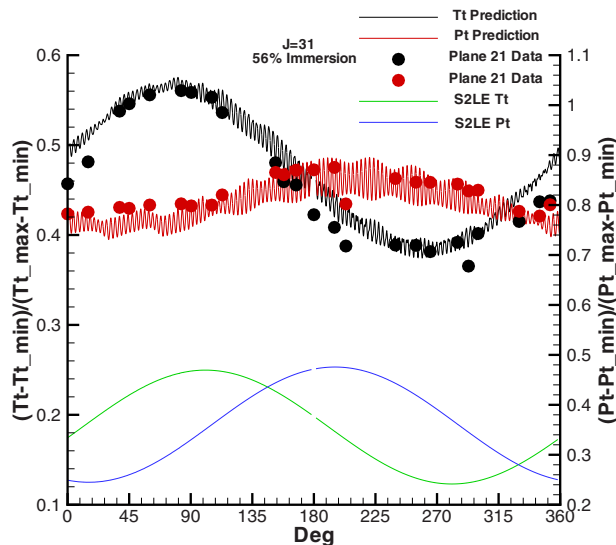
Fig. 14 Comparison of calculated *Pt* and *Tt* profiles with data at 55% immersion

The difference between the prediction and experimental data in total temperature is very encouraging. Recall also that the inlet boundary conditions at Stator-2 were approximations based on fitting a sine wave to Stator-2 leading edge measurements and will affect the magnitude of the prediction at Rotor-3 and Stator-3.

Figures 13–15 show the additional phase shift in total temperature distortion that occurred between Stator-2 inlet and Stator-3 exit at 91% immersion and 55% immersion but not at 7.3% immersion. The total pressure distortion remained in phase and was attenuated between Stator-2 inlet and Stator-3 exit at all three immersions. The total temperature distortion magnitude increased through the fan at all immersions.

6 Discussion of Results

The significant circumferential phase difference between the PT and TT distortion was observed in experimental data and the CFD simulations for both fans. Similar findings were reported by Mazzawy [4], and the phase difference was attributed to angular fluid particle displacement. There were also thoughts relating the phase
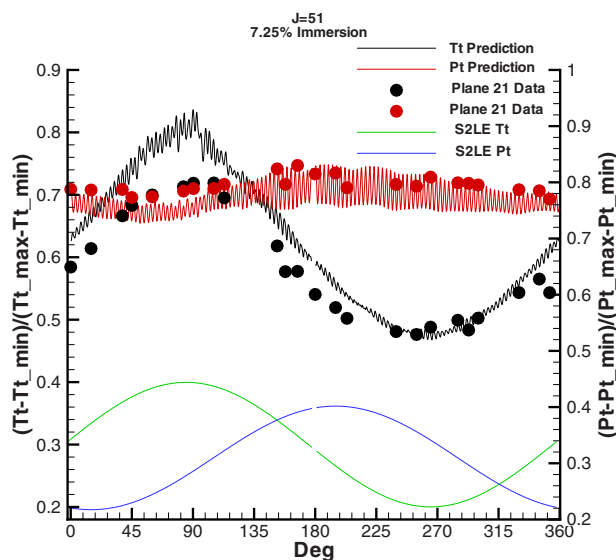

Fig. 15 Comparison of calculated *Pt* and *Tt* profiles with data at 7.3% immersion

difference to fluid inertia as described by Hynes and Greitzer [5]. These phenomena do exist in the flow, but are not found to be adequate to explain the total temperature phase difference at Stator-1 inlet. For the first fan model, the total temperature distortion was generated by Rotor-1 that is subjected to a nonuniform discharge pressure (see Fig. 10). For the second fan model, the total temperature distortion was imposed as a boundary condition upstream of Stator-2 based on measurement at Stator-2 inlet. Furthermore, TT distortion generation by the Rotor-3 was evident and the phase of the total temperature distortion was slightly shifted by Rotor-3. The amount of shifting in phase is different at different immersions, as shown in Figs. 13–15.

Attempt is made in this section to probe further for the mechanism. Separated views of the static temperature and absolute velocity (the quantities defining total temperature) for the first fan model are plotted in Fig. 16 at an upstream and downstream location for Rotor-1 at midspan. The Rotor-1 upstream location is located within the axial gap of the IGV and the Rotor-1 (black solid circles in plot). The Rotor-1 downstream location is located within the axial gap of the Rotor-1 and the Stator-1. The plots are taken from a time-accurate snapshot at an arbitrary time and are obviously marred by the passing Rotor-1 shocks at the upstream location and by the Rotor-1 wakes at the downstream location. The main profiles, however, stay stationary in the absolute frame of reference, and can be used as an alternative to time-averaged profiles. At the downstream location, Fig. 16 reveals that the static temperature determines the total temperature phasing observed in Fig. 5 since the Rotor-1 exit velocity profile is relatively flat. To probe further, static pressure and density profiles are plotted and shown in Fig. 17. The Rotor-1 discharge pressure profile has a visible phase difference (about 30 deg) from the inlet profile. The density profile, on the other hand, has a less visible phase shift (about 4 deg). The density distortion is noteworthy since it is often neglected in previous distortion analysis. Both profiles at Rotor-1 exit shift in the opposite direction of rotation. Following the equation of state, the static temperature can be modeled using two sinusoidal functions in the general form of $(1+\lambda_p \cos(\theta + \phi_p))/(1+\lambda_\rho \cos(\theta + \phi_\rho))$, where λ_p and λ_ρ are the relative amplitudes of pressure and density, and ϕ_p and ϕ_ρ are the phase shifts of pressure and density relative to the incoming profiles. When λ_p and λ_ρ are comparable, a small change in phase angles between ϕ_p and ϕ_ρ (about 26 deg in this case) could result in a large shift of the resultant temperature profile.

Compared to the static pressure profile at Rotor-1 exit, the total pressure profile does not exhibit the phase shift (see Fig. 5). The reason is that the absolute Mach number profile (not shown) at Rotor-1 exit has a mirrored shape of the local static temperature profile (produced by a relatively flat velocity profile and the static temperature profile, shown in Fig. 16). When the static pressure and Mach number are combined, the resultant total pressure profile is "shifted" back to almost the same phasing as the incoming total pressure profile.

From the perspective of fan response, the phase difference of Rotor-1 inlet and exit pressure profiles causes Rotor-1 loading variation along the circumference. This implies that the pressure and temperature rise across Rotor-1 varies in the circumference. Larger pressure rise in the 0–180 deg range is shown in Fig. 17, corresponding to temperature rise in the 0–180 deg range shown in Fig. 16. For inviscid flow, pressure and temperature changes are expressed as $C_p \Delta T = \Delta p / \rho$, and density variation could be a significant factor. This line of analysis is further extended in Part II of this paper [18], in which the pressure and temperature rise of all three rotors are examined for the underlying mechanism of temperature distortion generation and transfer.

More analysis, especially those that related to swirl distortions for both fan models, was also carried out but reported separately in Ref. [19].
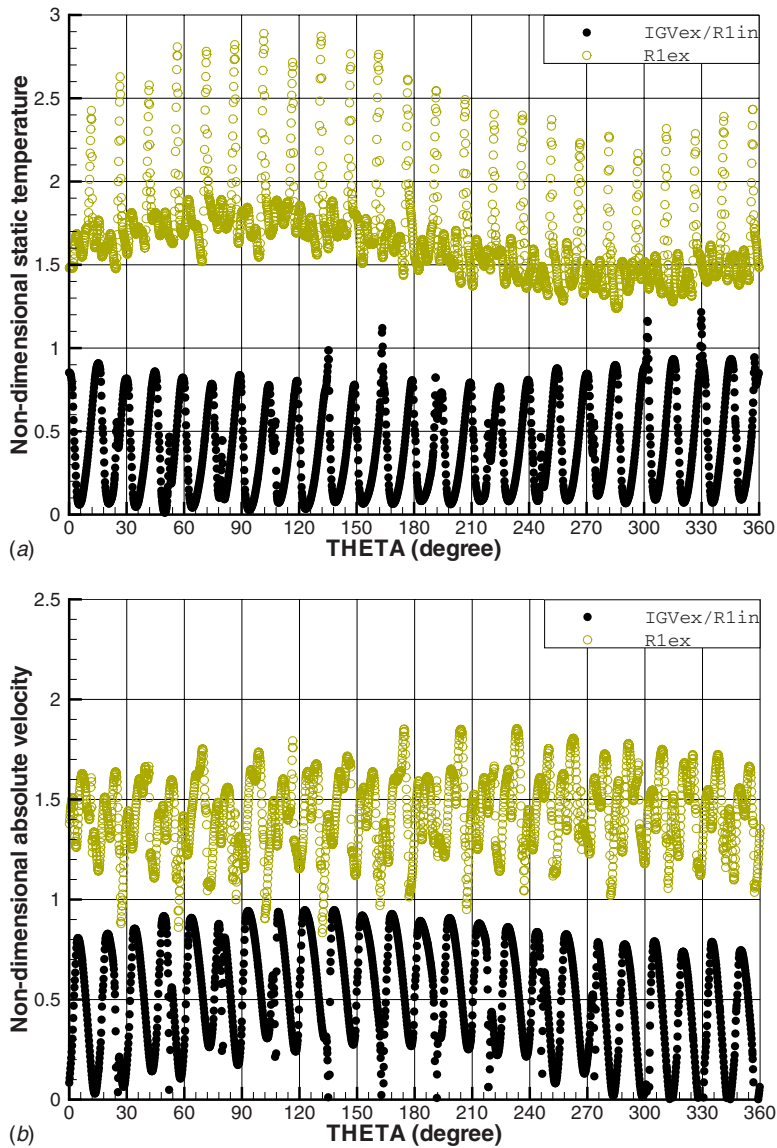
Fig. 16 Circumferential profiles of static temperature (top) and absolute velocity (bottom) at an upstream and downstream location of Rotor-1 at midspan. Reference location is Rotor-1 inlet at midspan.

7 Conclusions

Unsteady RANS calculations were successfully applied to predict the 1/rev inlet total pressure distortion transfer in the front block of one fan and the rear block of another fan. The following conclusions were drawn from the analysis of the numerical results and the comparisons of CFD to engine test data.

1. An unsteady RANS CFD procedure was demonstrated by making use of high-performance computing. No reduced order modeling was involved in this procedure. High performance computing allows full annulus simulations to be obtained in an acceptable time frame to be of benefit to the engine design process.

2. With careful consideration of grid and boundary conditions, the unsteady RANS CFD code PTURBO was shown to be capable of predicting temperature distortion generation and transfer of total pressure distortion in two different fans. Validation with total pressure and total temperature experimental data showed that the simulations predicted the proper magnitude and phase of distortion transfer and generation.

The magnitudes were predicted within 3.5% or better. Casing statics were compared upstream and downstream of Rotor-1 and showed that the static pressure rise and phase across the rotor were accurately captured. This represents a major step forward in distortion transfer prediction and resolving the circumferential details of distortion transfer and generation.

3. The 90 deg circumferential phasing difference between the pressure distortion and the generated temperature distortion in the first fan was accurately predicted. Experimental data from the second fan show a similar phase shift of 90 deg present at the leading edge of Stator-2. A smaller phase shift in total temperature continues through Rotor-3. The total temperature distortion was magnified and the total pressure distortion was attenuated.

4. Analysis of the simulations from both fans models showed that static temperature dominated the total temperature phasing. Both pressure rise and density variation in the fan circumference need to be considered to understand the temperature distortion generation.
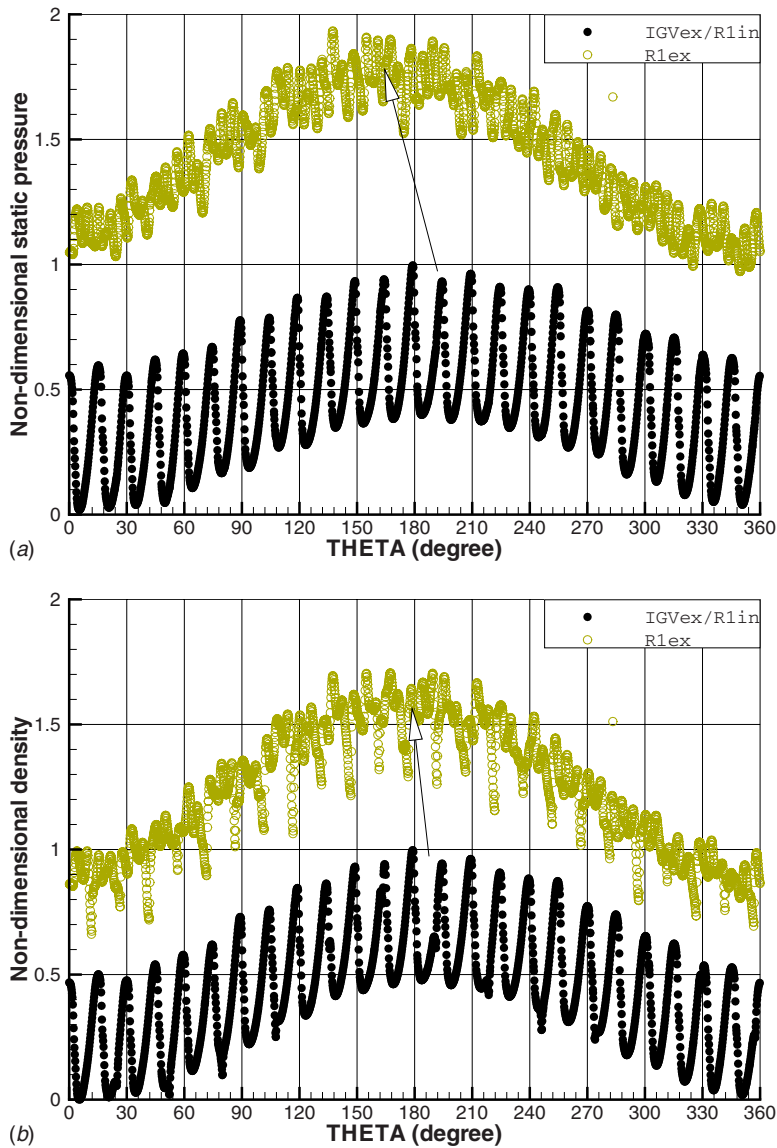
Fig. 17 Circumferential profiles of static pressure (top) and density (bottom) at an upstream and downstream location of Rotor-1 at midspan. Reference location is Rotor-1 inlet at midspan.

Nomenclature

PTA, PT, Pt = absolute total pressure
PS, Ps, p = static pressure
TTA, TT, Tt = absolute total temperature
TS, Ts = static temperature
θ, r, z = engine tangential, radial, and axial coordinates
b = blade chord length
u = axial velocity of the fluid
ρ = density of the fluid
s = entropy
h = enthalpy
C_p = fluid specific heat at constant pressure
ω = engine wheel speed

Subscripts

avg, ave = time average or engine circumferential average
min = minimum value in engine circumference
max = maximum value in engine circumference

local = local value at a specific immersion

References

[1] Roberts, F., Plourde, G., and Surakula, F., 1968, "Insights Into Axial Compressor Response to Distortion," AIAA Paper No. 68-565.

[2] Reid, C., 1969, "The Response of Axial Flow Compressors to Intake Flow Distortion," ASME Paper No. 69-GT-29.

[3] Plourde, G., and Stenning, A., 196, "The Attenuation of Circumferential Inlet Distortion in Multi-Stage Axial Compressors," AIAA Paper No. 67-415.

[4] Mazzawy, R., 1977, "Multiple Segment Parallel Compressor Model for Circumferential Flow Distortion," ASME J. Eng. Power, **99**, pp. 288–296.

[5] Hynes, T., and Greitzer, E., 1987, "A Method for Assessing Effects of Circumferential Flow Distortion on Compressor Stability," ASME J. Turbomach., **109**, pp. 371–379.

[6] Chue, R., Hynes, T., Greitzer, E., Tan, C., and Longley, J., 1989, "Calculation of Inlet Distortion Induced Compressor Flow Field Instability," Int. J. Heat Fluid Flow, **10**(3), pp. 211–223.

[7] Cumpsty, N. A., 1989, *Compressor Aerodynamics*, Longman Group UK Ltd., London, England.

[8] Longley, J. P., 1990, "Measured and Predicted Effects of Inlet Distortion on Axial Compressors," ASME Paper No. 90-GT-214.

[9] Longley, J. P., and Greitzer, E. M., 1992, "Inlet Distortion Effects in Aircraft Propulsion System Integration," *Steady and Transient Performance Prediction of Gas Turbine Engines*, AGARD-LS-183, Advisory Group for Aerospace Research and Development, Neuilly-Sur-Seine (France), NATO Research and Technology Organization.

[10] Hirai, K., Kodama, H., Nozaki, O., Kikuchi, K., Tamura, A., and Matsuo, Y., 1997, "Unsteady Three-Dimensional Analysis of Inlet Distortion in Turbomachinery," AIAA Paper No. 97-2735.

[11] Gong, Y., 1998. "A Computational Model for Rotating Stall Inception and Inlet Distortions in Multistage Compressor," Ph.D. thesis, Massachusetts Institute of Technology, Cambridge, MA.

[12] Hale, A., Davis, M., and Sirbaugh, J., 2004, "A Numerical Simulation Capability for Analysis of Aircraft Inlet—Engine Compatibility," ASME Paper No. GT-2004-53473.

[13] Chima, R. V., 2006. "A Three-Dimensional Unsteady CFD Model of Compressor Stability," ASME Paper No. GT2006-90040.

[14] Ryman, J. F., O'Brien, W. F., and Rabe, D. C., 2003, "Multi-Stage Fan and Compressor Transfer of Inlet Total Pressure Distortion With Emphasis on High Cycle Fatigue," AIAA Paper No. 2003-4979.

[15] Cousins, W. T., 2003. "Inlet Distortion Testing and Analysis of a High-Bypass Ratio Turbofan Engine," ISABE Paper No. 2003-1110.

[16] Chen, J. P., and Celestina, M. L., 1994. "A New Procedure for Simulating Unsteady Flows Through Turbomachinery Blade Passages," ASME Paper 94-GT-151.

[17] Chen, J. P., and Briley, W. R., 2001, "A Parallel Flow Solver for Unsteady Multiple Blade Row Turbomachinery Simulations," International Gas Turbine and Aeroengine Congress, ASME Paper No. GT2001-348,.

[18] Yao, J., Gorrell, S. E., and Wadia, A. R., 2010, "High-Fidelity Numerical Analysis of Per-Rev-Type Inlet Distortion Transfer in Multistage Fans—Part II: Entire Component Simulation and Investigation," ASME J. Turbomach., **132**, p. 041015.

[19] Yao, J., Gorrell, S. E., and Wadia, A. R., 2007. "A Time-Accurate CFD Analysis of Inlet Distortion Induced Swirl in Multistage Fans," AIAA Paper No. 2007-5059.